



First demonstration of in-beam performance of bent Monolithic Active Pixel Sensors

ALICE ITS project¹



ARTICLE INFO

Keywords:

Monolithic Active Pixel Sensors (MAPS)
Solid state detectors
Bent sensors

ABSTRACT

A novel approach for designing the next generation of vertex detectors foresees to employ wafer-scale sensors that can be bent to truly cylindrical geometries after thinning them to thicknesses of 20–40 μm . To solidify this concept, the feasibility of operating bent MAPS was demonstrated using $1.5\text{ cm} \times 3\text{ cm}$ ALPIDE chips. Already with their thickness of 50 μm , they can be successfully bent to radii of about 2 cm without any signs of mechanical or electrical damage. During a subsequent characterisation using a 5.4 GeV electron beam, it was further confirmed that they preserve their full electrical functionality as well as particle detection performance.

In this article, the bending procedure and the setup used for characterisation are detailed. Furthermore, the analysis of the beam test, including the measurement of the detection efficiency as a function of beam position and local inclination angle, is discussed. The results show that the sensors maintain their excellent performance after bending to radii of 2 cm, with detection efficiencies above 99.9% at typical operating conditions, paving the way towards a new class of detectors with unprecedented low material budget and ideal geometrical properties.

1. Introduction

The precision of barrel vertex detectors is mainly determined by three contributions: their radial distance to the interaction point, their material budget, and their intrinsic sensor resolution. In order to achieve hermiticity, they are typically built out of detector staves placed in layers around the beam pipe. This arrangement effectively sets a practical limit on the first two parameters. ALICE, for instance, achieves an average radial position of 24 mm and a material budget of $0.3\%X_0$ for its new Inner Tracking System (ITS2) [1]. More than 80% of the material is due to the support structure, and the average distance is determined by the chip's active area in $r\phi$ -directions of 1.3 cm together with the need of some overlap to detect particles traversing the detector at various angles.

A way to drastically improve these figures of merit is to use truly cylindrical detection layers made of wafer-size chips. This would not only allow placing them closer to the beam pipe, but would also largely suppress the need for the support structure, and in turn would substantially minimise the material budget to essentially that of the sensor itself. This idea is the gist of the ITS3, a proposal by the ALICE Collaboration for a novel vertex detector consisting of curved, wafer-scale, ultra-thin silicon sensors arranged in perfectly cylindrical layers, with the innermost layer positioned at a radial distance of only 18 mm from the nominal interaction point [2].

A major R&D milestone towards these new detectors is the proof of concept of bent Monolithic Active Pixel Sensor (MAPS). Using readily available ALPIDE chips (the MAPS of the ALICE ITS2 [3–5], Section 2),

mechanical (Section 2.1) and electrical (Section 2.3) studies as well as a beam test with 5.4 GeV electrons (Sections 3–5) were carried out.

The goal of these measurement is to verify the correct electrical functionality of the circuit after bending, and to quantify a possible performance degradation, caused e.g. by threshold shifts or worsening of charge collection and detection efficiencies.

2. The bent ALPIDE chip

The ALPIDE sensor was developed by the ALICE Collaboration for its Inner Tracking System (ITS2) [3–5]. The chip is produced in the 180 nm CMOS imaging process of TowerJazz [6] featuring a 25 μm -thick epitaxial layer. Here, chips thinned to 50 μm have been used.

ALPIDE features a matrix of 1024×512 (column \times row) pixels with binary output. The pixels of size $26.88\ \mu\text{m} \times 29.24\ \mu\text{m}$ are organised in double-columns, each one having 1024 pixels (Fig. 1). The central part of each double-column is occupied by priority encoding circuits which propagate the addresses of the hit pixels to the digital circuitry on the chip periphery. The digital periphery occupies an area of $1.2\text{ mm} \times 30\text{ mm}$ along the edge of the chip. A series of aluminum pads on top of the digital periphery, close to the edge of the chip, provide the electrical interface to the chip.

Each ALPIDE pixel contains the sensing diode connected to its individual and continuously active front-end amplifier, shaper, discriminator, and multiple-event buffer. It also contains analog and digital

¹ See Appendix for the complete list of authors.

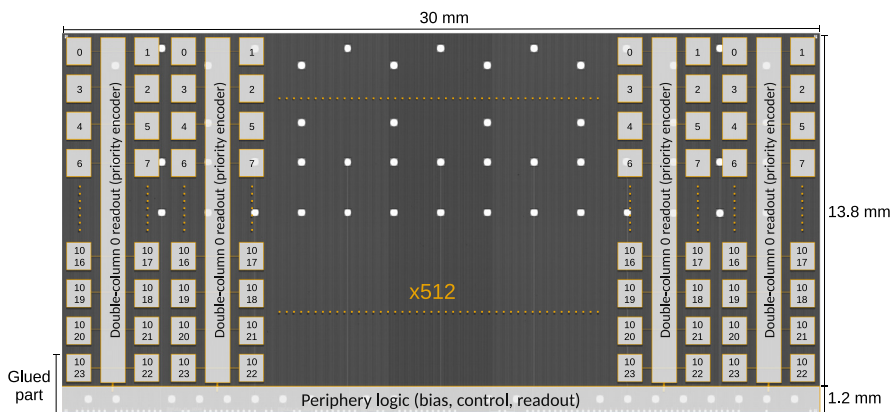


Fig. 1. Layout of the ALPIDE pixel matrix. The pixels are organised in double-columns, each featuring a priority encoder circuit which propagates the addresses of the hit pixels to the periphery logic. The aluminum pads providing the electrical interface to the chip are located on the top of the periphery logic.

testing circuitry, allowing the measurement of the charge threshold by injecting a programmable test charge into the sensing node. The threshold can be changed for all pixels simultaneously by adjusting the amplifier parameters [3–5,7].

At this point, it is worth pointing out that the pixel matrix itself – which will be the part of the chip that is bent, see below – is a highly integrated circuit, including analog and digital circuitry totaling to order of 200 transistors per pixel cell and with a dense metal routing.

2.1. Bending procedure

A procedure to bend the chip in a progressive and reversible manner was specifically developed and is described hereafter. The long edge hosting the bonding pads and the periphery logic as well as an about 0.8 mm-wide strip of the pixel matrix (Fig. 1) is glued onto a carrier board for a 2 mm-wide section (Fig. 2(a)) by means of acrylic adhesive.² The chip is then wire-bonded to the carrier card, before realising the bending procedure. The bonding area remains flat and well secured throughout and after the procedure. The rest of the chip is left unattached and is lightly compressed between two layers of 120 μm -thick polyimide foil (Fig. 2(a)). The polyimide foil layers are attached to two lateral wheels (Fig. 2(a)) that can be moved in parallel to the short edge of the chip by means of a micrometer-precision positioning system (not visible in pictures). By moving the wheels towards the chip, the polyimide foils wrap around them, and bend the chip into a cylindrical shape. Once the desired curvature is achieved, the wheels position is fixed using Ω -shaped aluminum fixtures (visible in Fig. 2(a)). Alternatively, the micro-positioning system allows reverting to the flat or any intermediate position.

2.2. Curvature measurement

A 3-D metrological mapping of the chip surface was performed using a Coordinate Measuring Machine (CMM) before and after the testbeam measurement. The carrier card with the bent chip (Fig. 2(a)) was laid on the measurement table and a series of data points was measured with an optical head, providing a resolution of 5 μm in the table plane, and 80 μm on the height. The data point series was projected on the axis given by the short edge of the chip, as reported in Fig. 3, and fitted with a circle of radius r and origin in y_0 , with y_0 parameter describing the flat (glued) part of the chip. The fit procedure provided an average curvature radius of 16.9 mm before and 24.4 mm after the testbeam. The change in curvature is attributed to a relaxation of the polyimide foil holder before, during, or after the testbeam. Therefore, it was expected, and later confirmed by the data analysis (Section 5.1), that the curvature during the testbeam measurement was in-between the two CMM measurements.

2.3. Performance comparison before and after bending

To verify the electrical functionality, i.e. the analogue in-pixel circuitry and the digital column circuitry propagating the position of the hit pixels to the periphery, the chip was characterised in terms of number of non-responsive pixels, pixel thresholds, noise and fake-hit rate before and after the bending. The tested parameters are unchanged or their change is negligible, as is shown in Fig. 4 for the pixel threshold distribution, as an example.

Since this measurement exercises the full analog and digital processing chain of the chip and hence it does not only show that its front-end performance is unaffected by the bending, but also that the whole circuit – notably the in-matrix distributed digital readout network – is still in full function.

3. Testbeam set-up

The testbeam was carried out at the DESY testbeam facility beam line 24 [8], with a 5.4 GeV electron beam.

The beam telescope comprised 6 reference planes with flat ALPIDE chips. The bent device under test (DUT) was placed in the middle, with 3 reference planes on each side (Fig. 2(b) and Fig. 5). The vertical (y) position of the DUT was adjustable, allowing the fine tuning of the position of the DUT with respect to the beam.

The telescope and DUT were operated without active cooling at room temperature or slightly above due to self-heating of the setup.

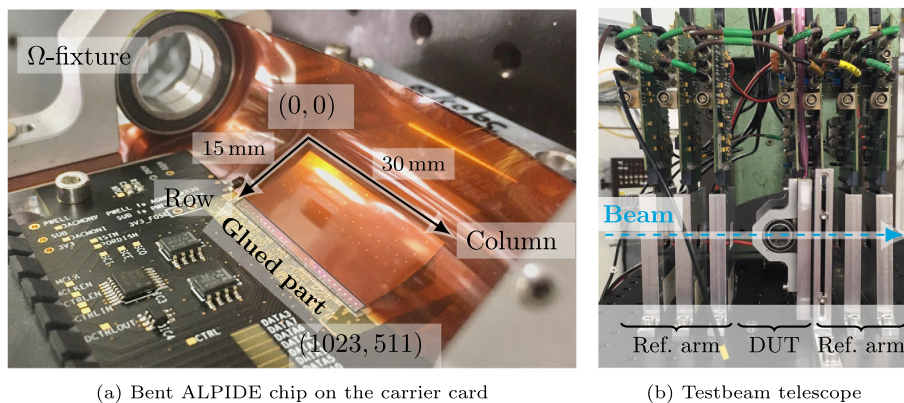
The trigger was given by the coincidence of the discriminated output of two photomultiplier tubes (operated in the plateau regime) connected to two scintillators with size of 4 cm \times 5 cm, placed in front and behind the telescope. The triggering logic includes an event separation time of 100 μs and a past protection time of 50 μs , i.e. a veto on triggering in 50 μs following a scintillator output signal. The latter is added to avoid the pile-up as the ALPIDE in-pixel amplifier pulse can reach lengths of few tens of μs for very low threshold values [7].

The data acquisition was based on the EUDAQ framework [9]. A total of 176 runs, with at least 300k events each, were collected with different threshold settings and DUT positions.

4. Analysis tools and methods

Data were processed in the Corryvreckan test beam reconstruction software framework [10] by fitting straight lines to clusters found in the six reference planes and interpolating the tracks to the DUT. Event and track quality selection criteria were applied to ensure a clean data sample: precisely one track per event, good straightness ($\chi^2/\text{NDF} < 3$) of the track, and track points on each reference plane. Pixels with too large overall firing quantities (more than 1000 times the average; $\ll 1\%$ of the total pixels are affected) were ignored. On the DUT,

² 3M™ Adhesive Transfer Tape 467MP, <https://www.3-m.com/>.



(a) Bent ALPIDE chip on the carrier card

(b) Testbeam telescope

Fig. 2. The ALPIDE chip glued to the carrier card and held in bent position via two polyamide foils attached to the aluminum wheels (a) and the same arrangement inserted in the testbeam telescope consisting of six flat ALPIDE tracking planes (b).

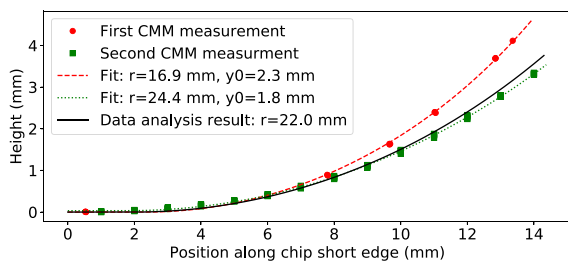


Fig. 3. Curvature radius measured using a Coordinate Measuring Machine (CMM) and obtained from the testbeam data analysis (Section 5.1).

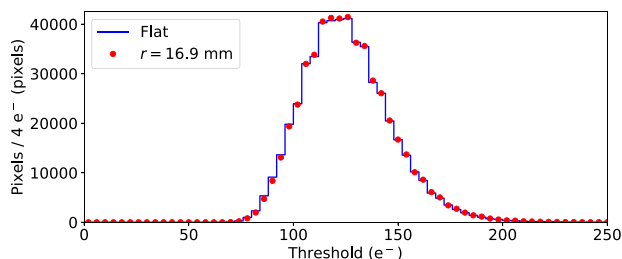


Fig. 4. Pixel threshold distribution before and after bending the chip. The difference between the two measurements is negligible.

clusters with a distance of below 250 μm are matched to the track. The size of the search window was chosen as large as possible without impacting the statistics due to border exclusion regions. Given the one track per event requirement, the implemented trigger logic (Section 3), extremely low ALPIDE noise [3–5] and masking of noisy pixels, as well as former experience of beam tests with the same telescope, the fraction of clusters wrongly associated to a track is considered negligible.

The reference planes and the DUT are aligned to each other by software using a track-cluster residual minimisation, allowing the planes to move in x , y and to rotate around z . In a second iteration, the DUT alone was allowed to rotate around the other two axes and to move in z . In this last step, also the bending radius was allowed to be varied by the optimisation algorithm, resulting in a data-driven estimate of this quantity.

As discussed in Section 2.1, a part of the DUT containing a small fraction of the pixel matrix (≈ 30 rows) is glued to the carrier card. Due to the additional scattering from the carrier card, the sensitivity to the geometrical model used to describe the DUT is reduced in this region. Therefore, the bent shape of the DUT was approximated as a purely cylindrical segment in this analysis, without considering the flat part (y_0 in Section 2.2).

The efficiency of the DUT is then estimated by the fraction of tracks with associated clusters. The relative uncertainties are obtained by calculating the Clopper–Pearson interval.

5. Results

5.1. Cluster size, curvature radius and residuals

The results presented in this section are based on the data from a single measurement (run) where the DUT was operated at the nominal conditions, i.e. at a threshold of 100 e^- . To fully illuminate the DUT, the measurement was repeated in two DUT positions with a relative shift along the y -axis (row direction, see Fig. 5) of 2.5 mm, of which the lower one is shown here.

The positions of all the clusters on the DUT and those associated to a track are shown in Fig. 6. In the area near row 512, where the chip is glued to the carrier card, less associated clusters are found given the lower number of reconstructed tracks (Section 4). On the opposite side, i.e. near row 0, there are no clusters associated to tracks due to the relative position of the DUT with respect to the reference planes. The associated cluster distribution is further affected by the relative position of the reference planes; given the precision of mechanical alignment of the chip position of a few millimeters and the requirement of a hit in all reference planes for the reconstructed tracks, the effective area illuminated by the beam is smaller than the chip size. This effect is mostly notable as a drop-off in the number of associated clusters near rows 100 and 400.

From the data in Fig. 6 (left), the average cluster sizes were calculated for 16 groups of 32 rows and shown in Fig. 7. With the increasing row number, the incident angle of the beam with respect to the DUT decreases, thus decreasing the particle path in the active volume and therefore the deposited charge, finally resulting in smaller clusters.

The least squares optimisation of the cylindrical model (Section 4) yielded the DUT radius of (22 ± 1) mm. The uncertainty on the radius takes into account the variation of the least square optimisation result over all the runs. The impact of the beam profile on this result was evaluated using two sets of tracks: the first uniformly distributed over the illuminated DUT surface and the second using all tracks with associated clusters on the DUT, as visible in Fig. 6 (right). Both sets result in the same curvature radius.

The mean and the RMS of the residuals in the column and row directions are shown in Fig. 8. A systematic effect of magnitude of up to 35 μm can be observed in the row residual mean, most prominent in the unattached corners of the DUT and along the glued edge. The RMS of both residuals above row 400 increases, which is compatible with the position of the carrier card, i.e. can be attributed to the increase of the multiple scattering. Also an increase of the row residual RMS with decreasing row number can be observed, a trend compatible with the cluster size increase that is observed for larger beam incident angles (Fig. 7).

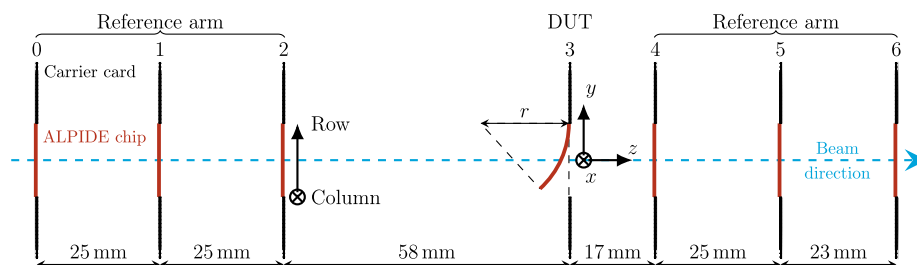


Fig. 5. Sketch of the beam telescope with the bent DUT sandwiched between six flat ALPIDE reference planes. The DUT position can be translated in the y -direction.

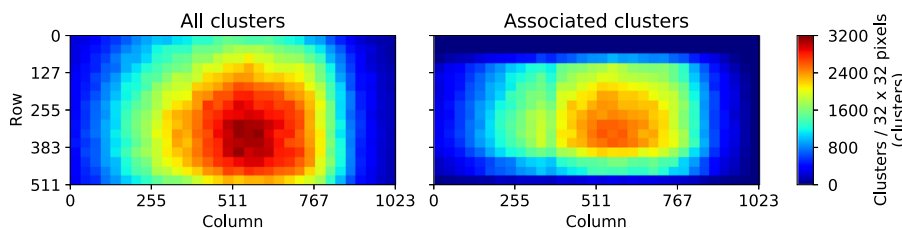


Fig. 6. Distributions of all the clusters on the DUT (left) and of those associated to the tracks (right). Fewer clusters are associated to tracks in columns 376–381 due to exclusion of a dead double column.

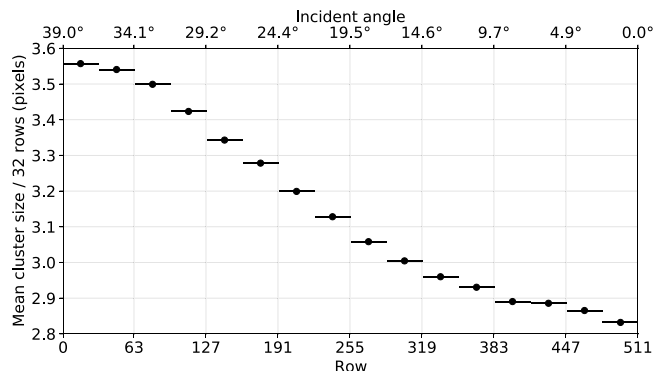


Fig. 7. Average cluster size as a function of row and corresponding incident angle. The average cluster size decreases with the increasing row number; as the track incident angle decreases, so does the interaction volume and thus the deposited charge.

5.2. Detection efficiency

The data from different runs were combined to evaluate the efficiency at different thresholds and over the entire DUT surface. The border region equivalent to the track association window size (250 μm i.e. 9 pixels), as well as the same width region on each side of a dead double-column (columns 369 to 388) were excluded from the efficiency calculation.

Figs. 9 and 10 show the inefficiency as a function of row, beam incident angle, and threshold. Each data point corresponds to at least 8k tracks, and over 48k tracks for central rows (given the beam profile, Fig. 6). For threshold above $100e^-$ (the nominal operating point of ALPIDE), the efficiency increases with increasing beam incident angle (decreasing row number). Below $100e^-$, the inefficiency is generally lower than 10^{-4} , showing that an excellent detecting performance is retained.

6. Summary

The feasibility of bent MAPS was demonstrated for the first time. In particular, 50 μm -thick ALPIDE chips were measured in the laboratory and in a beam test while being bent to radii of about 22 mm. They show

no sign of any deterioration in operation. Their charge discrimination thresholds remain unaffected by the bending and detection efficiencies are measured to largely exceed 99.9% without any visible systematic degradation across the full chip surface.

These very encouraging results do not only mark an important milestone in the R&D carried out for the ALICE ITS3, but generally open the way to highly integrated, silicon-only, bent sensor arrangements. A new class of detector designs featuring ideal geometries and yielding unprecedented performance figures is at reach.

The presented results are accompanied by a number of systematic studies on the electromechanical integration, aiming at different bending radii, using wafer-scale chips, studying the effect of temperature variations and gradients (including “aging”), as well as the effect of non-uniform thicknesses onto the geometry. These are followed by the ALICE ITS3 project, and are subject of future publications.

Declaration of competing interest

The authors declare that they have no known competing financial interests or personal relationships that could have appeared to influence the work reported in this paper.

Acknowledgments

The measurements leading to these results have been performed at the Test Beam Facility at DESY Hamburg (Germany), a member of the Helmholtz Association (HGF). We would like to thank the coordinators at DESY for their valuable support of this testbeam measurement and for the excellent testbeam environment.

We thank the Corryvreckan developers, especially S. Spannagel and L. Huth for their precious support.

B.M. Blidaru acknowledges support by the HighRR research training group [GRK 2058].

F. Krizek acknowledges support by the Ministry of Education, Youth and Sports of the Czech Republic project [LM2018104].

G. Usai acknowledges support by the project “STITCHED MAPS” funded by MIUR, Italy – grant PRIN 2017C7KLSX – Italy

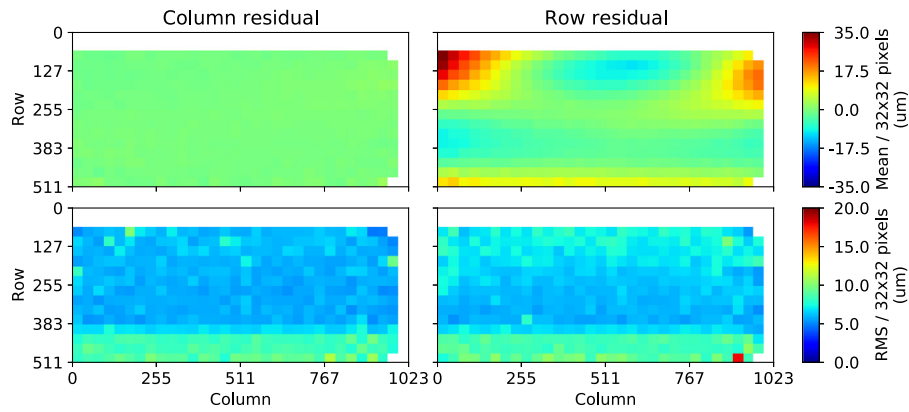


Fig. 8. Mean (top panels) and RMS (bottom panels) of the column and row residuals. The cylindrical model description is compatible with the data within 35 μm .

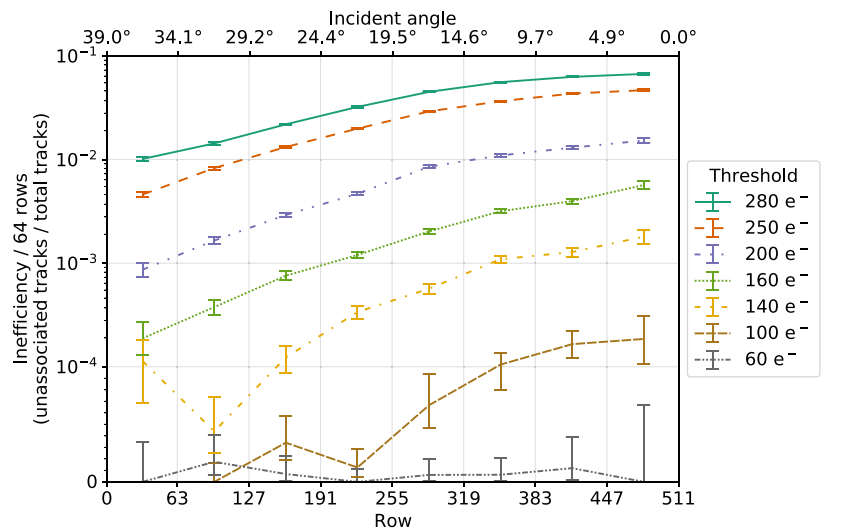


Fig. 9. Inefficiency as a function of row and corresponding incident angle. The error bars indicate the statistical uncertainty. Each data point corresponds to at least 28k tracks. Note the partially logarithmic vertical scale.

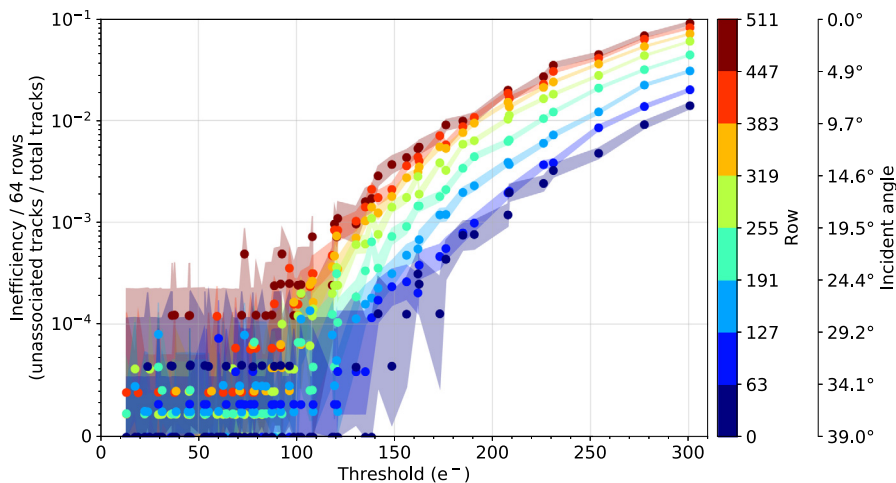


Fig. 10. Inefficiency as a function of threshold for different rows and incident angles. The dark circles represent the calculated efficiency and the shaded areas the statistical uncertainty. Each data point corresponds to at least 8k tracks. Note the partially logarithmic vertical scale.

Appendix. The ALICE ITS project

G. Aglieri Rinella¹⁸, M. Agnello¹⁴, B. Alessandro²⁷, F. Agnese⁴⁷, R.S. Akram³, J. Alme⁷, E. Anderssen³², D. Andreou³³, F. Antinori²⁵, N. Apadula³², P. Atkinson³⁴, R. Baccomi²⁸, A. Badalà²⁴, A. Balbino¹⁴,

C. Bartels⁴⁵, R. Barthel³³, F. Baruffaldi¹², I. Belikov⁴⁷, S. Beole¹⁰, P. Becht^{38,39}, A. Bhatti³, M. Bhopal³, N. Bianchi²¹, M.B. Blidaru^{38,39}, G. Boca¹³, J. Bok²⁹, G. Bonomi⁴⁹, M. Bonora¹⁸, M. Borri³⁴, V. Borshchov¹, E. Botta¹⁰, G.E. Bruno^{37,17}, M. Buckland⁴⁵, S. Bufalino¹⁴, M. Cai^{12,2}, P. Camerini⁹, P. Cariola²², F. Catalano¹⁴, C. Ceballos

Sanchez²², I. Chakaberia³², M. Chartier⁴⁵, F. Colamaria²², D. Colella^{37,22}, A. Collu³², M. Concas^{18,27}, G. Contin⁹, S. Costanza¹³, P. Cui², A. Dainese²⁵, J.B. Dainton⁴⁵, L. De Cilladi¹⁰, C. De Martin⁹, G. De Robertis²², W. Deng², A. Di Mauro¹⁸, Y. Ding², M. Durkac⁴², D. Elia²², M.R. Erstad⁷, M. Faggin¹², F. Fan², A. Fantoni²¹, P. Fecchio¹⁴, A. Feliciello²⁷, G. Feofilov⁴⁰, A. Ferk¹⁸, J. Ferencei³⁵, G. Fiorenza^{18,22}, A.N. Flores⁴³, E. Fragiaco²⁸, D. Gajanana³³, A. Gal⁴⁷, C. Gao², C. Gargiulo¹⁸, P. Gianotti²¹, P. Giubilato¹², A. Grant³⁴, L. Greiner³², A. Grelli³⁰, O.S. Groettvik^{18,7}, F. Grosa^{18,27}, C. Guo Hu⁴⁷, R. Hannigan⁴³, J.A. Hasenbichler¹⁸, H. Helstrup¹⁹, H. Hillemanns¹⁸, C. Hills⁴⁵, P. Hindley³⁴, B. Hippolyte⁴⁷, B. Hofman³⁰, G.H. Hong⁵⁰, G. Huang², J.P. Iddon^{18,45}, H. Ilyas^{3,18}, M.A. Imhoff⁴⁷, A. Isakov³⁵, A. Jadlovska⁴², S. Jadlovska⁴², J. Jadlovska⁴², S. Jaelani³⁰, T. Johnson³², A. Junique¹⁸, P. Kalinak³¹, A. Kalweit¹⁸, M. Keil¹⁸, Z. Khabanova³³, H. Khan³, B. Kim⁴, C. Kim⁴, J. Kim⁵⁰, J. Kim⁵⁰, T. Kim⁵⁰, J. Klein¹⁸, A. Kluge¹⁸, C. Kobdaj⁴¹, A. Kotliarov³⁵, I. Králik³¹, F. Krizek³⁵, T. Kugathasan¹⁸, C. Kuhn⁴⁷, P.G. Kuijer³³, S. Kushpil³⁵, M.J. Kweon²⁹, J.Y. Kwon²⁹, Y. Kwon⁵⁰, P. La Rocca¹¹, A. Lakrathok⁴¹, R. Langoy⁴⁶, P. Larionov²¹, E. Laudi¹⁸, T. Lazareva⁴⁰, R. Lea^{49,9}, R.C. Lemmon³⁴, X.L. Li², J. Lien⁴⁶, B. Lim⁴, S.H. Lim⁴, S. Lindsay⁴⁵, A. Liu⁵, J. Liu², J. Liu⁴⁵, M. Lunardon¹², G. Luparello²⁸, M. Lupi¹⁸, M. Mager¹⁸, A. Maire⁴⁷, Q.W. Malik⁶, G. Mandaglio^{16,24}, V. Manzarri²², Y. Mao², G.V. Margagliotti⁹, C. Markert⁴³, D. Marras²³, P. Martinengo¹⁸, S. Masciocchi³⁹, M. Maserà¹⁰, A. Masoni²³, A. Mastroserio^{48,22}, P.F.T. Matuoka^{21,44}, G. Mazza²⁷, F. Mazzaschi¹⁰, M.A. Mazzoni^{26,†}, F. Morel⁴⁷, V. Muccifora²¹, A. Mulliri⁸, L. Musa¹⁸, S.V. Nesbo¹⁹, D. Nesterov⁴⁰, J. Norman⁴⁵, J. Park²⁹, R.N. Patra¹⁸, C. Pastore²², H. Pei², X. Peng², S. Piano²⁸, C. Pinto¹¹, S. Pisano²¹, S. Politano¹⁴, E. Prakasa²⁰, F. Prino²⁷, M. Protsenko¹, M. Puccio¹⁸, A. Rachevski²⁸, L. Ramello¹⁵, F. Rami⁴⁷, I. Ravasenga³³, A. Rehman⁷, F. Reidt¹⁸, F. Riggi¹¹, K. Røed⁶, D. Röhrich⁷, F. Ronchetti²¹, A. Rosano^{16,24}, M.J. Rossewijk³³, A. Rossi²⁵, R. Rui⁹, R. Russo³³, R. Sadikin²⁰, V. Sarritzu²³, J. Schambach^{36,43}, S. Senyukov⁴⁷, J.J. Seo²⁹, R. Shahoyan¹⁸, S. Shaikat³, S. Siddhanta²³, M. Sitta¹⁵, R.J.M. Snellings³⁰, W. Snoeys¹⁸, A. Songmoolnak⁴¹, J. Sonneveld³³, F. Soramel¹², M. Suljic¹⁸, S. Sumowidagdo²⁰, D. Sun², X. Sun², G.J. Tambave⁷, G. Tersimonov¹, M. Tkacik⁴², M. Toppi²¹, A. Trifiro^{16,24}, S. Trogolo^{18,12}, V. Trubnikov¹, R. Turrisi²⁵, T.S. Tveter⁶, I. Tymchuck¹, K. Ullaland⁷, M. Urioni⁴⁹, G.L. Usai⁸, N. Valle¹³, L.V.R. van Doremalen³⁰, T. Vanat³⁵, J.W. Van Hoorne¹⁸, M. Varga-Kofarago¹⁸, A. Velure¹⁸, D. Wang², Y. Wang², J. Wikne⁶, J.R. Wright⁴³, R. Xu², P. Yang², Z. Yin², I.-K. Yoo⁴, J.H. Yoon²⁹, S. Yuan⁷, V. Zaccolo⁹, E. Zhang³², X. Zhang², V. Zherebchevskii⁴⁰, D. Zhou², J. Zhu², Y. Zhu², G. Zinoviev¹, N. Zurlo⁴⁹

¹ Bogolyubov Institute for Theoretical Physics, National Academy of Sciences of Ukraine, Kiev, Ukraine

² Central China Normal University, Wuhan, China

³ COMSATS University Islamabad, Islamabad, Pakistan

⁴ Department of Physics, Pusan National University, Pusan, Republic of Korea

⁵ Department of Physics, University of California, Berkeley, California, United States

⁶ Department of Physics, University of Oslo, Oslo, Norway

⁷ Department of Physics and Technology, University of Bergen, Bergen, Norway

⁸ Dipartimento di Fisica dell'Università and Sezione INFN, Cagliari, Italy

⁹ Dipartimento di Fisica dell'Università and Sezione INFN, Trieste, Italy

¹⁰ Dipartimento di Fisica dell'Università and Sezione INFN, Turin, Italy

¹¹ Dipartimento di Fisica e Astronomia dell'Università and Sezione INFN, Catania, Italy

¹² Dipartimento di Fisica e Astronomia dell'Università and Sezione INFN, Padova, Italy

¹³ Dipartimento di Fisica e Nucleare e Teorica, Università di Pavia and Sezione INFN, Pavia, Italy

¹⁴ Dipartimento DISAT del Politecnico and Sezione INFN, Turin, Italy

¹⁵ Dipartimento di Scienze e Innovazione Tecnologica dell'Università del Piemonte Orientale and INFN Sezione di Torino, Alessandria, Italy

¹⁶ Dipartimento di Scienze MIFT, Università di Messina, Messina, Italy

¹⁷ Dipartimento Interateneo di Fisica 'M. Merlin' and Sezione INFN, Bari, Italy

¹⁸ European Organization for Nuclear Research (CERN), Geneva, Switzerland

¹⁹ Faculty of Engineering and Science, Western Norway University of Applied Sciences, Bergen, Norway

²⁰ Indonesian Institute of Sciences, Jakarta, Indonesia

²¹ INFN, Laboratori Nazionali di Frascati, Frascati, Italy

²² INFN, Sezione di Bari, Bari, Italy

²³ INFN, Sezione di Cagliari, Cagliari, Italy

²⁴ INFN, Sezione di Catania, Catania, Italy

²⁵ INFN, Sezione di Padova, Padova, Italy

²⁶ INFN, Sezione di Roma, Rome, Italy

²⁷ INFN, Sezione di Torino, Turin, Italy

²⁸ INFN, Sezione di Trieste, Trieste, Italy

²⁹ Inha University, Incheon, Republic of Korea

³⁰ Institute for Gravitational and Subatomic Physics (GRASP), Utrecht University/Nikhef, Utrecht, Netherlands

³¹ Institute of Experimental Physics, Slovak Academy of Sciences, Košice, Slovakia

³² Lawrence Berkeley National Laboratory, Berkeley, California, United States

³³ Nikhef, National institute for subatomic physics, Amsterdam, Netherlands

³⁴ Nuclear Physics Group, STFC Daresbury Laboratory, Daresbury, United Kingdom

³⁵ Nuclear Physics Institute of the Czech Academy of Sciences, Řež u Prahy, Czech Republic

³⁶ Oak Ridge National Laboratory, Oak Ridge, Tennessee, United States

³⁷ Politecnico di Bari and Sezione INFN, Bari, Italy

³⁸ Physikalisches Institut, Ruprecht-Karls-Universität Heidelberg, Heidelberg, Germany

³⁹ Research Division and ExtreMe Matter Institute EMMI, GSI Helmholtzzentrum für Schwerionenforschung GmbH, Darmstadt, Germany

⁴⁰ St. Petersburg State University, St. Petersburg, Russia

⁴¹ Suranaree University of Technology, Nakhon Ratchasima, Thailand

⁴² Technical University of Košice, Košice, Slovakia

⁴³ The University of Texas at Austin, Austin, Texas, United States

⁴⁴ Universidade de São Paulo (USP), São Paulo, Brazil

⁴⁵ University of Liverpool, Liverpool, United Kingdom

⁴⁶ University of South-Eastern Norway, Tonsberg, Norway

⁴⁷ Université de Strasbourg, CNRS, IPHC UMR 7178, F-67000 Strasbourg, France

⁴⁸ Università degli Studi di Foggia, Foggia, Italy

⁴⁹ Università di Brescia and Sezione INFN, Brescia, Italy

⁵⁰ Yonsei University, Seoul, Republic of Korea

[†] deceased

References

- [1] ALICE Collaboration, Technical design report for the upgrade of the ALICE inner tracking system, *J. Phys. G: Nucl. Part. Phys.* 41 (8) (2014) 087002, <http://dx.doi.org/10.1088/0954-3899/41/8/087002>, <https://doi.org/10.1088%2F0954-3899%2F41%2F8%2F087002>.
- [2] ALICE Collaboration, Letter of Intent for an ALICE ITS Upgrade in LS3, *Tech. Rep. CERN-LHCC-2019-018*. LHCC-I-034, CERN, Geneva, 2019, URL <https://cds.cern.ch/record/2703140>.
- [3] M. Šuljić, ALPIDE: the monolithic active pixel sensor for the ALICE ITS upgrade, *J. Instrum.* 11 (11) (2016) C11025, <http://dx.doi.org/10.1088/1748-0221/11/11/c11025>, <https://doi.org/10.1088%2F1748-0221%2F11%2F11%2Fc11025>.
- [4] G. Aglieri Rinella, The ALPIDE pixel sensor chip for the upgrade of the ALICE inner tracking system, *Nucl. Instrum. Methods Phys. Res. A* 845 (2017) 583–587, <http://dx.doi.org/10.1016/j.nima.2016.05.016>, Proceedings of the Vienna Conference on Instrumentation 2016, URL <http://www.sciencedirect.com/science/article/pii/S0168900216303825>.

- [5] M. Mager, ALPIDE, the monolithic active pixel sensor for the ALICE ITS upgrade, *Nucl. Instrum. Methods Phys. Res. A* 824 (2016) 434–438, <http://dx.doi.org/10.1016/j.nima.2015.09.057>, Frontier Detectors for Frontier Physics: Proceedings of the 13th Pisa Meeting on Advanced Detectors, URL <http://www.sciencedirect.com/science/article/pii/S0168900215011122>.
- [6] TowerJazz, <http://www.towersemi.com/>, URL <http://www.towersemi.com/>, Last accessed on 25/01/2021.
- [7] D. Kim, G.A. Rinella, C. Cavicchioli, N. Chanlek, A. Collu, Y. Degerli, A. Dorokhov, C. Flouzat, D. Gajanana, C. Gao, F. Guilloux, H. Hillemanns, S. Hristozkov, A. Junique, M. Keil, M. Kofarago, T. Kugathasan, Y. Kwon, A. Lattuca, M. Mager, K. Sielewicz, C.M. Tobon, D. Marras, P. Martinengo, G. Mazza, H. Mugnier, L. Musa, T. Pham, C. Puggioni, F. Reidt, P. Riedler, J. Rousset, S. Siddhanta, W. Snoeys, M. Song, G. Usai, J.V. Hoorne, P. Yang, Front end optimization for the monolithic active pixel sensor of the ALICE inner tracking system upgrade, *J. Instrum.* 11 (02) (2016) C02042, <http://dx.doi.org/10.1088/1748-0221/11/02/c02042>.
- [8] R. Diener, J. Dreyling-Eschweiler, H. Ehrlichmann, I. Gregor, U. Kötz, U. Krämer, N. Meyners, N. Potylitsina-Kube, A. Schütz, P. Schütze, M. Stanitzki, The DESY II test beam facility, *Nucl. Instrum. Methods Phys. Res. A* 922 (2019) 265–286, <http://dx.doi.org/10.1016/j.nima.2018.11.133>, URL <http://www.sciencedirect.com/science/article/pii/S0168900218317868>.
- [9] P. Ahlburg, et al., EUDAQ–A data acquisition software framework for common beam telescopes, *J. Instrum.* 15 (01) (2020) P01038, <http://dx.doi.org/10.1088/1748-0221/15/01/p01038>, <https://doi.org/10.1088%2F1748-0221%2F15%2F01%2Fp01038>.
- [10] D. Dannheim, K. Dort, L. Huth, D. Hynds, I. Kremastiotis, J. Krüger, M. Munker, F. Pitters, P. Schütze, S. Spannagel, T. Vanat, M. Williams, Corryvreckan: A modular 4D track reconstruction and analysis software for test beam data, *J. Instrum.* 16 (03) (2021) P03008, <http://dx.doi.org/10.1088/1748-0221/16/03/p03008>.